Check for updates

High Power Laser Science and Engineering, (2026), Vol. 14, e52, 12 pages.
doi:10.1017/hpl.2026.10154

HIGH POWER LASER SCIENCE AND ENGINEERING

RESEARCH ARTICLE

High-repetition-rate, all-reflective optical guiding and electron acceleration in helium using an off-axis axicon

Jiří Šišma[1,2], Michal Nevrkla[1,2], Filip Vitha[1,2], Sebastian Lorenz[1], Illia Zymak[1], Alžběta Špádová[1,2], Andrea Kollárová[1,2], Matěj Jech[1,3], Alexandr Jančárek[1,2], Davorin Peceli[1], Carlo M. Lazzarini[1], Leonardo V. N. Goncalves[1], Gabriele M. Grittani[1], Sergei V. Bulanov[1], Jaron E. Shrock[4], Ela Rockafellow[4], Ari J. Sloss[4], Bo Miao[4], Scott W. Hancock[4], and Howard M. Milchberg[4,5]

[1] *ELI Beamlines Facility, The Extreme Light Infrastructure ERIC, Dolní Břežany, Czech Republic*

[2] *Faculty of Nuclear Sciences and Physical Engineering, Czech Technical University in Prague, Prague, Czech Republic*

[3] *Faculty of Information Technology, Czech Technical University in Prague, Prague, Czech Republic*

[4] *Institute for Research in Electronics and Applied Physics and Department of Physics, University of Maryland, College Park, Maryland, USA*

[5] *Department of Electrical and Computer Engineering, University of Maryland, College Park, Maryland, USA*

(Received 7 December 2025; revised 2 April 2026; accepted 30 April 2026)

Abstract

We present recent results on high-power guiding and laser wakefield acceleration in the ELectron Beam Accelerator (ELBA) beamline at ELI Beamlines, using the L3-HAPLS laser system (13 J, 30 fs, 0.2 Hz). By employing self-waveguiding in a 20 cm plasma channel in helium, we achieved stable acceleration of electron beams to energies of approximately 5 GeV. A novel all-reflective optical setup, including an off-axis reflective axicon, enabled efficient acceleration at 0.2 Hz and guiding at repetition rates up to 3.3 Hz. This compact single laser, single-compressor implementation of plasma channels for electron acceleration stabilizes electron pointing and enhances energy gain without requiring modifications to the laser system, paving the way for broader adoption of the technology across user facilities.

Keywords: high-power laser guiding; laser wakefield acceleration; plasma channels

1. Introduction

Laser wakefield acceleration (LWFA) enables compact generation of high-energy electron beams[1], which are driving advances in several fields. LWFA electron beams are being used to develop compact free-electron lasers (FELs) that produce ultrashort, high-brilliance X-ray and infrared (IR) radiation[2–4]. These electron beams also serve as sources for secondary particles and radiation, including high-quality positron beams[5,6], high-energy photons[7–10] and even muons[11–13], enabling applications in fundamental physics[14,15], such as probing techniques[16–18], as well as in radiotherapy[19–21]. Furthermore, the extremely high acceleration gradients achievable with LWFA – 10^3 times higher than in conventional radio frequency (RF) accelerators[22], allowing acceleration to multi-GeV energies in sub-meter-scale plasma[23–26] – open the door to next-generation high-energy particle colliders, potentially reducing the size and cost of future TeV-scale accelerators[27].

The electron energy gain in LWFA is primarily limited by laser diffraction, pulse depletion and dephasing. To overcome diffraction and maximize energy gain, several guiding techniques have been developed. One approach is self-guiding, where an ultra-high-intensity laser pulse creates its own plasma channel via relativistic and ponderomotive self-focusing, balancing diffraction and enabling propagation over several Rayleigh lengths[24,26,28]. However, it is a nonlinear process that is highly dependent on plasma density, which can limit controllability, stability and efficiency. In contrast, pre-formed plasma channels, created in advance using methods such as optical-field ionization (OFI)[25,29–43] or capillary discharge[23,44–48], provide a stable, low-density guiding structure without reliance on nonlinear propagation

Correspondence to: J. Šišma, ELI Beamlines Facility, The Extreme Light Infrastructure ERIC, Za Radnicí 835, Dolní Břežany 25241, Czech Republic. Email: jiri.sisma@eli-laser.eu.

© The Author(s), 2026. Published by Cambridge University Press in association with Chinese Laser Press. This is an Open Access article, distributed under the terms of the Creative Commons Attribution licence (https://creativecommons.org/licenses/by/4.0), which permits unrestricted re-use, distribution and reproduction, provided the original article is properly cited.

Downloaded from https://www.cambridge.org/core. 19 Nov 2026 at 08:25:42, subject to the Cambridge Core terms of use.

effects. In LWFA, this enables propagation over much longer distances (from tens of centimeters to meters) and supports higher electron energies[25,41,42,48] by enabling acceleration at lower plasma densities. Pre-formed channels also offer better control over the plasma density profile, matched laser spot size and overall stability, reducing shot-to-shot fluctuations and improving beam quality[39,49].

The first plasma waveguides were demonstrated in high-density plasma using inverse Bremsstrahlung heating[50,51]. This heating mechanism is inefficient and unsuitable for the low plasma densities required for multi-GeV LWFA[25,41,42], as it cannot achieve on-axis densities below 10^{17} cm^{-3}. However, extending the method to use density-independent OFI as the heating mechanism[30–32,34,35,52], together with auxiliary ionization of the neutral shock to form the cladding[29,34,35,37,38], has enabled the production of highly confining, meter-scale plasma waveguides with on-axis densities below 10^{17} cm^{-3}. These free-standing waveguides are immune to laser damage, longitudinally tunable[39,49] and can reliably reach the low densities required for high-energy acceleration[25,41,42] using gas jet technology[38,53,54]. In contrast, capillary-based waveguides are limited by their fixed geometry and susceptibility to laser-induced damage[55], and the inability to reach densities as low as approximately 1×10^{17} cm^{-3}[48]. Electron energies of up to 8 GeV have been achieved using capillary discharge waveguides enhanced with auxiliary laser heating[48].

Advances in laser technology have enabled the use of hydrodynamically expanded OFI plasma columns to form plasma waveguides, allowing for longer acceleration lengths and improved control over plasma profiles[29,31,34,35,37]. However, at low target gas density, a single femtosecond channel-forming pulse may not create the core and adequately confine cladding of a plasma waveguide structure by itself. Instead, it ionizes a plasma column causing a hydrodynamic expansion with a plasma 'core' on-axis and neutral-density shock expanding outwards. A secondary pulse is required to ionize the neutral-density shock to form the 'cladding' and establish the refractive index required for guiding[29,34,35,37]. Two main techniques have been developed: the '2-Bessel' method[34], which uses a secondary higher-order Bessel beam to ionize the neutral shock of the OFI channel, allowing guiding of a high- or low-intensity pulse; and the 'self-waveguiding' technique[29,35,37], which simplifies the process by using the leading edge of an intense pulse to ionize the neutral shock, forming the waveguide structure for itself as it propagates, simultaneously driving the wake. Both methods have recently been implemented with phase front correction[25,56,57] to produce high-fidelity Bessel beams, which are crucial for stable and efficient plasma channel formation. Single-stage plasma accelerators have achieved electron energies up to 10 GeV, using nanoparticle-assisted self-guided LWFA with 130 J on target[26] and self-waveguiding of the LWFA driver pulse with 18 J[42] and 21 J[41] on target.

We present a new modification of the self-waveguiding technique that employs post-compressor splitting of the channel-forming pulse from an initially square transverse profile (super-Gaussian in each dimension) femtosecond laser pulse. This approach primarily relies on reflective optics, thereby avoiding heat deposition in transmissive components and preventing beam distortions caused by B-integral effects in short pulses. For the first time in high-power LWFA experiments, we implemented an off-axis reflective axicon[58], offering straightforward alignment and reduced risk of laser damage compared to traditional on-axis back-reflective configurations[34,35]. The all-reflective setup preserved the compressed pulse duration after the axicon and enabled the formation of plasma channels in helium, which requires laser intensities above 9×10^{15} W/cm^2 for full ionization[52,59]. Previous studies have shown that the plasma channel properties of OFI-generated plasmas can be maintained even at kHz repetition rates[60], confirming the suitability of this approach for future high-repetition-rate accelerators and colliders. In our experiments, we implemented the self-waveguiding LWFA scheme of Ref. [25], where 5 GeV electron acceleration was previously demonstrated in hydrogen. Using an all-reflective geometry, we achieved stable optical guiding of high-intensity laser pulses in a 3 cm plasma channel at 3.3 Hz, and, for the first time in helium, we demonstrated electron acceleration to energies up to 5 GeV in a 20 cm plasma channel. The use of helium as the working gas provides a safer and more easily pumped alternative to hydrogen, which was commonly used in similar experiments[25,39,41,42] due to its lower ionization threshold. This work demonstrates that the proposed approach is both adaptable and efficient for laser user facilities where laser system modification is limited by operational constraints, while enabling maximized electron energy gain compared to conventional self-guiding methods. Owing to its single-compressor implementation, the scheme is well suited for future compact muon sources.

2. Experimental setup

The experiments were performed at the ELBA (ELectron Beam Accelerator) beamline[61] using the L3-HAPLS Ti:sapphire laser system at the ELI Beamlines facility in the Czech Republic. In these experiments, the laser delivered linearly polarized, 30 fs pulses with peak power of 400 TW at a central wavelength of 810 nm, providing up to 13 J of energy at 0.2 Hz repetition rate, or up to 8 J at 3.3 Hz. The beam had a rectangular super-Gaussian profile with dimensions of 214 mm × 214 mm.

In Figure 1, the laser beam enters the auxiliary chamber from the left and is first reflected by a high-reflectivity (HR) dielectric mirror[62] (M1). Two pick-off mirrors are then used to split small portions of the pulse to form two auxiliary beams: a channel-forming beam and a probe beam.

Downloaded from https://www.cambridge.org/core. 19 Nov 2026 at 08:25:42, subject to the Cambridge Core terms of use.

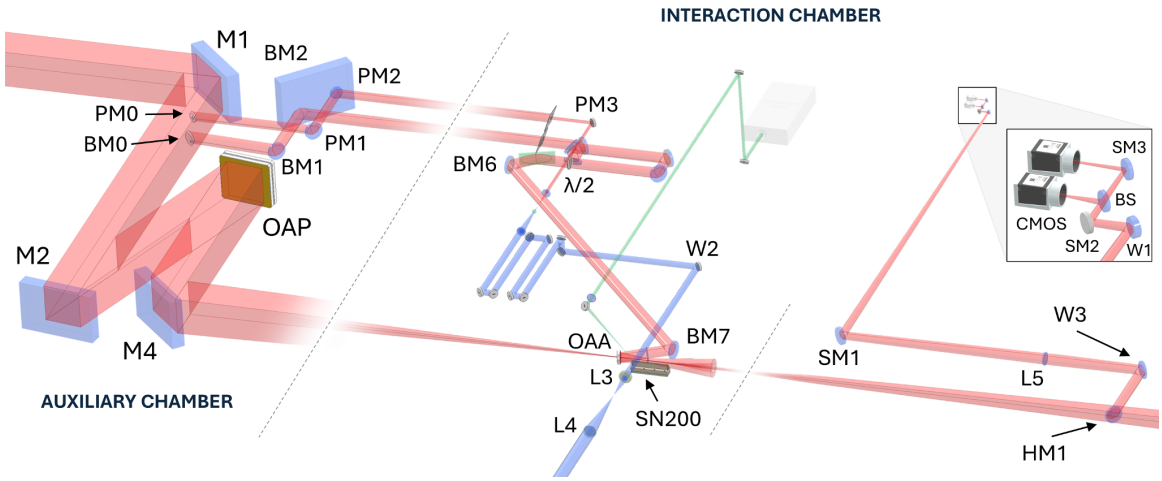


Figure 1. Experimental setup overview. The laser beam enters the auxiliary chamber from the left and is reflected by mirror M1. Two pick-off mirrors split small portions of the pulse to form the channel-forming and probe beams, while the main pulse continues as the LWFA drive beam. The channel-forming beam is routed through the auxiliary chamber and directed into the interaction chamber toward the off-axis axicon (OAA) positioned above the gas jet SN200, where it generates the plasma channel. The probe beam is guided through its delay line and diagnostic path, and the drive beam is focused by the off-axis parabola (OAP) into the interaction region for laser wakefield acceleration. The high-power focal-spot and guided-beam diagnostics are shown on the right-hand side of the interaction chamber and include a mirror with a central aperture (HM1), an uncoated wedge (W3), an imaging lens (L5) and a mirror (SM1) that directs the attenuated pulse out of the chamber to CMOS cameras. The green beam path indicates a separate nanosecond laser system used in independent experiments to test alternative injection mechanisms. A detailed description of the setup is provided in Section 2.

The main portion of the beam continues to an HR mirror (M2) and a 20° off-axis parabola (OAP) with a 10 m focal length. The reflected beam is directed by mirror M4 through the central aperture of the off-axis axicon (OAA), focusing above the gas jet. Mirror M4 also enables fine alignment between the channel entrance and the drive beam without requiring OAP adjustments, thereby preventing focal-spot distortion and ensuring stability during extended operation.

The channel-forming (Bessel) beam is separated by a 45° silver-coated elliptical mirror (BM0) with a 66 mm minor diameter, extracting up to 1.1 J from the initial 13 J pulse. This beam is subsequently guided by a dielectric 4-inch mirror (BM1) and an HR mirror (BM2) into the interaction chamber, connected to the auxiliary chamber by a 6.2 m long beam-transport tube. Within this section, the beam can be apodized using ceramic apertures to achieve the desired diameter and suppress diffraction. All mirrors BM0–BM2 are motorized to allow smooth, remote alignment over long distances, ensuring stability and reproducibility throughout the experiment.

In the remaining beamline (see Figure 2), enhanced silver-coated mirrors (BM3–BM7 and delay-line mirrors) were employed. The single-compressor scheme and size of the vacuum chambers constrain the delay to a maximum of 5.6 ns between the LWFA drive pulse and the Bessel beam, adjustable via an 840 mm single-pass delay-line stage. The initially linearly p-polarized channel-forming beam passes through a polarization-changing periscope (BM4–BM5) that rotates its polarization by 90° to work in a reflective attenuator configuration designed for s-polarization. A beam attenuator consisting of a half-wave plate ($\lambda/2$) and a reflective femtosecond thin-film polarizer (TFP) was implemented to enable precise control of the Bessel beam energy[40,42], providing flexibility in tuning the plasma waveguide parameters. The attenuator could be bypassed, allowing operation with only reflective components in the beam path suitable for high-repetition-rate operation. Data presented in this paper were taken without the attenuator installed.

Finally, mirrors BM6 and BM7 were used to align a 3-inch reflective 30° OAA with a 3° base angle ($\approx$ 105 mrad approach angle) and a 7 mm central aperture, which allows the LWFA drive beam to couple into the pre-formed density structure above a 20-cm-long supersonic slit-nozzle single-valve gas jet SN200. It is a supersonic slit-nozzle system developed at ELI Beamlines[53] for long laser–plasma-driven electron acceleration schemes. The nozzle is designed to produce a 20-cm-long region of uniform gas density above the slit, with minimal density variations along the flat-top profile. The system incorporates a gas reservoir and a set of flow deflectors positioned upstream of the nozzle throat to maintain a stable and uniform density distribution, even when operated with a single gas valve connected to the nozzle assembly. This nozzle system differs from previously reported designs[38,42,54] in that the gas is supplied through a single valve. This configuration significantly simplifies implementation of the system and allows the target to be operated using readily available commercial driver hardware. The trade-off, however, is a comparatively long valve-opening time ($\approx$10 ms), which is required for the gas density profile to fully develop prior to the arrival of the laser pulse.

Similarly, the probe beam was extracted from the main laser beam using a 2-inch elliptical, protected silver-coated

Downloaded from https://www.cambridge.org/core. 19 Nov 2026 at 08:25:42, subject to the Cambridge Core terms of use.

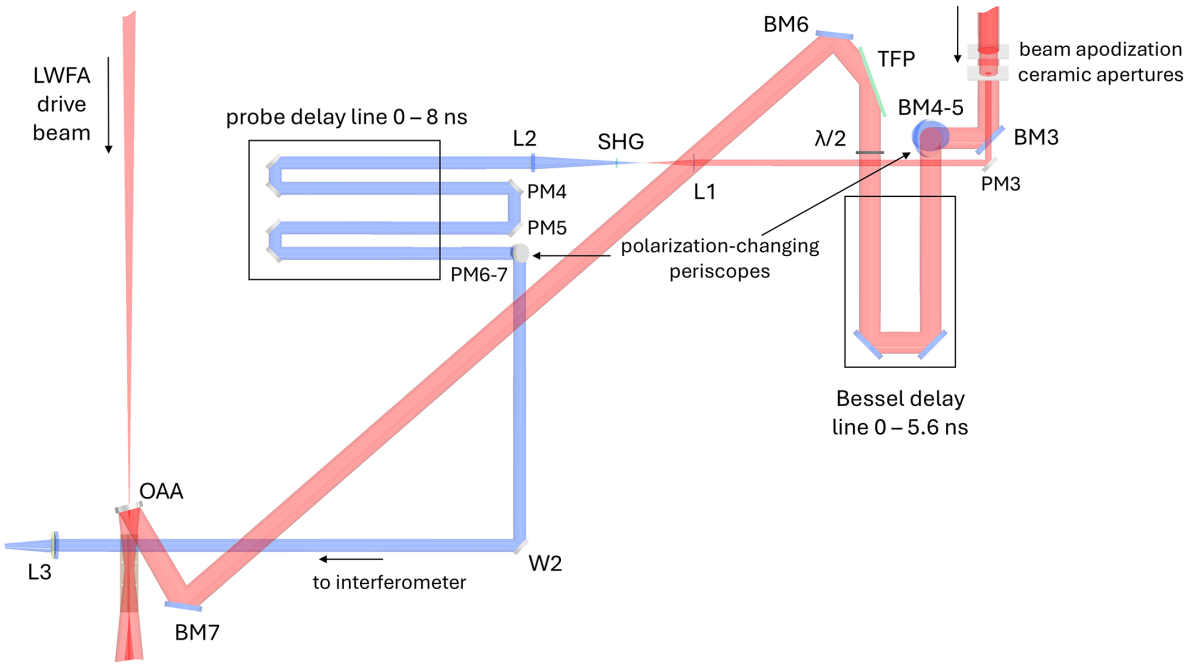


Figure 2. Schematic layout of the interaction chamber setup for the self-waveguided LWFA experiment. The final section of the optical system is shown, starting from mirror BM3, where the channel-forming (Bessel) beam enters the chamber, and including all subsequent mirrors BM3–BM7, the periscope, attenuator (half-wave plate, $\lambda/2$, and thin-film polarizer, TFP) and delay-line mirrors leading to the off-axis axicon (OAA) positioned above the 20 cm gas jet SN200. The LWFA drive beam passes through the axicon's central aperture and interacts with the plasma channel formed by the Bessel beam, while the probe beam is directed from its apodization aperture via mirror PM3 to the telescope (lenses L1 and L2) with an SHG BBO crystal, then through a delay line toward the interferometer for diagnostics. A detailed description of the setup is provided in Section 2.

mirror (PM0). It was then directed by a 4-inch enhanced silver-coated mirror (PM1) and a 3-inch dielectric mirror (PM2) toward the interaction chamber, where it was apodized using a ceramic aperture. The beam was subsequently reflected by a 2-inch protected silver-coated mirror (PM3) into a telescope consisting of a thin lens (L1) and an achromatic lens (L2), transmitting through a beta barium borate (BBO) crystal for second-harmonic generation (SHG) at 800 nm (see Figure 2). For the experimental results discussed in this paper, the fundamental (first harmonic) probe was used exclusively as the diagnostic beam.

The probe beam then passed through a double-pass, 600-mm-long delay-line stage, enabling precise timing of the probe pulse with respect to the drive pulse from –2 to +6 ns. This allowed temporal scanning of the plasma channel evolution from 0 to 8 ns by adjusting the Bessel beam delay.

Finally, the probe beam polarization was rotated using a polarization-changing periscope (PM6 and PM7), enabling the filtering of p-polarized scattered driver light, and then transmitted through an uncoated wedge (W2) into the interaction region. The transmitted beam was focused by a 3-inch, 200-mm-focal-length achromatic convex lens (L3), forming the first element of a Keplerian telescope that guided the beam out of the chamber through a large-aperture optical window. The beam was then collimated by another 3-inch, 400-mm-focal-length achromatic convex lens (L4) before entering a folded-wave Mach–Zehnder interferometer, where the image was focused onto a complementary metal–oxide–semiconductor (CMOS) camera with a 2× magnification.

The scanning interferometer system enables spatial scanning of the probe beam along the gas jet through synchronized motorized control of the wedge W2, the first lens L3 and the entire out-of-chamber interferometer assembly, including lens L4, allowing independent and repeatable positioning along the interaction region.

For the post-interaction diagnostics, we employed a high-power focal-spot and guided-mode diagnostic system consisting of a 4-inch drilled uncoated ultraviolet fused silica (UVFS) mirror (HM1) with a grinded back surface, a 4-inch uncoated wedged (W3) mirror, a 3-inch imaging lens (L5) with a 2000 mm focal length and a 4-inch protected silver-coated mirror (SM1). Outside the chamber, the beam was reflected by a 1-inch uncoated wedge (W1) and directed by a silver mirror (SM2) toward the first beam splitter (BS), which sent one portion to a CMOS camera imaging the focal plane. The second image was focused onto another CMOS camera monitoring the guided mode at the exit plane of the waveguide. The cameras used were spectrally sensitive in the visible and near-infrared (near-IR) range up to 1100 nm. Each UVFS reflection at 45° attenuates the p-polarized beam to 0.66% of the initial incident power at 800 nm. With three uncoated UVFS reflections, the beam is attenuated by a

Downloaded from https://www.cambridge.org/core. 19 Nov 2026 at 08:25:42, subject to the Cambridge Core terms of use.

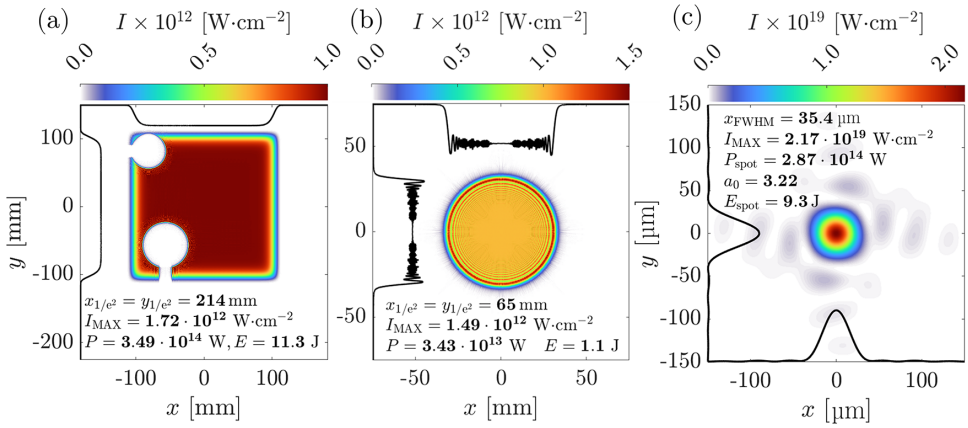


Figure 3. Simulations of laser beam wavefront splitting and the focal spot. (a) Wavefront of the LWFA drive beam after the pick-offs at the off-axis parabola (OAP). (b) Wavefront of the channel-forming beam after 12 m of free-space propagation at the axicon surface. (c) Focal spot of the LWFA drive beam (a) on target.

factor of 3×10^{-7}. To prevent detector saturation, absorptive neutral-density filters were placed in front of the cameras for additional attenuation with the total optical density ranging from 3 to 6, corresponding to attenuation factors from 10^{-3} to 10^{-6}.

The accelerated electron beam passed through a 10 mm central aperture in the first mirror HM1, positioned 3 m downstream from the nozzle exit (corresponding to a 3 mrad divergence). After exiting the chamber through a 1-mm-thick aluminum flange, it propagated toward a 1 mm tungsten slit, composed of 6-cm-thick blocks, placed directly in front of a 50-cm-long slit electromagnet operating at a uniform magnetic field of 0.6 T. A LANEX screen was mounted at the exit of the electromagnet and imaged by a CMOS camera equipped with a camera lens and a 546 nm bandpass filter with a 10 nm bandwidth for energy-spectrum diagnostics. The electron spectrometer was calibrated in charge using a conventional linac at energies of 6−20 MeV[63], and correction factors were applied to account for differences in the geometric arrangement of the setup.

We also employed top-view and side-view fluorescence diagnostics[38] consisting of CMOS cameras equipped with camera lenses, motorized neutral-density filter wheels and a helium line bandpass filter centered at 589 nm with a 10 nm bandwidth. The filter isolated the strong, well-separated helium emission line at 587.6 nm, corresponding to the 3d → 2p transition following recombination. To prevent laser light from reaching the detectors and to improve signal quality, IR cut filters were placed in front of the cameras (doubled IR cut at 645 nm with $< 1\%$ averaged transmission in the range of 690−1070 nm for the side-view camera and doubled IR cut at 710 nm with $< 10\%$ averaged transmission in the range of 740−1200 nm for the top-view camera). These diagnostics were used for fine alignment of the plasma column above the gas jet and to observe impurities in both the gas sheet and the Bessel beam intensity distribution. The resulting fluorescence signal represents the combined effects of the Bessel beam intensity profile along the propagation and gas density fluctuations or inhomogeneities.

3. Laser-splitting and focal-spot simulations

We performed laser beam-splitting and focal-spot simulations for an ideal super-Gaussian beam using the L3-HAPLS laser parameters to compare with the measured focal spots and to estimate the energy distribution in each pulse. In addition, we simulated the free-space propagation of the Bessel beam to study diffraction-induced distortions after approximately 12 m of propagation. To suppress the resulting diffraction pattern, a serrated aperture can be employed[64]. All simulations were carried out using VirtualLab Fusion 7.0.1[65] (fast physical-optics simulation software).

In Figure 3, we present simulations of the free-space propagation and focal spot of the LWFA drive beam. For a 13 J, 30.4 fs, 10th-order super-Gaussian pulse, the LWFA driver beam carries 11.3 J of energy (Figure 3(a)), while the channel-forming (Bessel) beam contains 1.1 J. The simulated propagation shows modulation in the near-field of the channel-forming beam intensity due to diffraction effects (Figure 3(b)). The remaining 0.5 J of energy was allocated to the probe beam. The resulting focal spot corresponding to the wavefront (in Figure 3(a)) is shown in Figure 3(c). The expected full width at half maximum (FWHM) is approximately equal to 35 µm, with a normalized vector potential of $a_0 = 3.22$ and a maximum energy in the zeroth diffraction order of 9.3 J, corresponding to 82.3% of total energy.

4. Experimental results

We have verified pulse compression in the experimental chamber by employing SPIDER (spectral phase interferometry for direct electric-field reconstruction)[66] to measure the

Downloaded from https://www.cambridge.org/core. 19 Nov 2026 at 08:25:42, subject to the Cambridge Core terms of use.

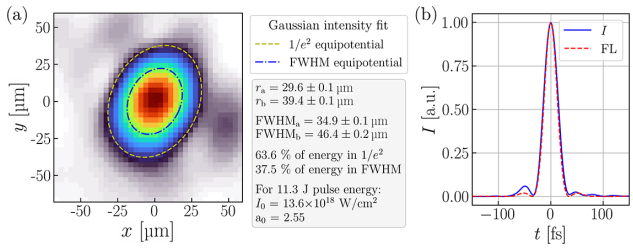


Figure 4. Laser beam measurements. (a) Low-power focal-spot image and corresponding analysis. (b) Laser pulse characterization using SPIDER measurement, where I denotes the measured intensity profile and FL denotes the Fourier-limited laser pulse, that is, the minimum pulse duration calculated from the measured spectral bandwidth, assuming a flat spectral phase.

femtosecond pulse duration, obtaining 30.4 fs (FWHM), as shown in Figure 4(b). The focal spot was characterized in the low-power regime (L3-HAPLS front-end) by mapping the total energy across the full image, resulting in the distribution presented in Figure 4(a). After noise subtraction, the focal spot was fitted with a Gaussian profile, yielding a minor-axis FWHM of 35 µm and a major-axis FWHM of 46 μm. The overall energy coupling within the beam radius ($1/e^2$) was estimated to be approximately 64% (7.2 J). For an ideal Gaussian intensity profile, the encircled energy within the $1/e^2$ radius is approximately 86.5% of the total energy. The retrieved normalized vector potential was $a_0 = 2.55$. Based on performed simulations, the Strehl ratio (defined as the ratio of measured to simulated a_0 in the focal region) was estimated to be 0.79.

4.1. *High-repetition-rate, high-power laser guiding*

We characterized high-power laser guiding at 0.2 Hz in a 20 cm helium plasma channel (Figure 5) and high-repetition-rate guiding at 3.3 Hz using a 3 cm supersonic slit nozzle (Figures 6 and 7). The shorter nozzle and reduced gas opening time were selected to limit the gas load in the interaction chamber, enabling sustained operation at 3.3 Hz while maintaining acceptable vacuum conditions. Figures 5(a) and 5(b) show high-power focal-spot images recorded through the gas sheet during active guiding and in vacuum at the focal plane, respectively. The transverse intensity profile of the zeroth-order Bessel beam J_0 is presented in Figure 5(c), yielding a first-zero radius of 2.83 ± 0.01 μm measured with a 5× finite-conjugate objective. The guided mode at the 20 cm exit plane is shown in Figure 5(d).

Figures 5(e)–5(g) provide a direct comparison of the focal-spot and guided-mode distributions on a common spatial scale. The guided-mode image in Figures 5(f) was obtained with the 3 cm nozzle (corresponding diagnostics shown in Figures 7). In both the 3 and 20 cm configurations, the guided mode becomes more circularly symmetric relative to the incident focal spot (Figures 5(b)). This behavior is consistent with suppression of higher-order mode content via leakage[35,67,68] and group velocity walkoff[39]. The residual light surrounding the central spot in Figures 5(f) is attributed to leakage from the waveguide.

High-repetition-rate guiding at 3.3 Hz was demonstrated using the 3 cm nozzle, as shown in Figure 7. Figure 6(a) presents the time evolution of the guided mode over a period of approximately equal to 20 minutes of operation at 3.3 Hz. Each shot is represented by a line-averaged intensity profile extracted from a fixed region centered on the guided mode (see Figure 5(f)). The guided energy deviation within a beam radius ($1/e^2$) is shown in Figure 6(b), together with the energy drift calculated as a moving average over a 60-shot window. The guided mode remains stable throughout the sequence for a laser pulse of approximately equal to 250 TW, with no evidence of long-term degradation. A small decrease in guided energy observed after 800 seconds is attributed to a drop in the gas valve backing pressure. The guiding was achieved at a backing pressure of 6 bar, corresponding to an average neutral density of approximately equal to 9.4×10^{17} cm^{-3} along the gas jet. The axial neutral-gas density profiles, measured via the top-view fluorescence diagnostic, are shown in Figure 7(b). A representative fluorescence image from this diagnostic is shown in Figure 7(a).

4.2. *Electron acceleration in helium*

We achieved electron acceleration in a 20 cm pre-formed helium plasma channel generated above the supersonic slit nozzle SN200, operated with a single valve and a 10 ms opening time limited by the vacuum pumping system. The neutral-density profiles measured along the gas jet are shown in Figure 5(i). The observed nonuniformity is attributed to the short opening time, during which the gas does not have sufficient time to develop the flat density distribution expected from the design. This behavior originates from the relatively large reservoir volume, designed to suppress turbulence and enable steady-state flow, but leading to a filling time comparable to the valve-opening duration. The nozzle was therefore operated in a transient flow regime. Future optimization will focus on reducing the reservoir volume and refining the internal geometry to enable faster filling and a more uniform density profile within the available opening time.

The highest-energy shots were obtained with 7.2 J contained within the $1/e^2$ focal-spot radius (see Figure 4(a)), for delays from 1.7 to 2.1 ns between the channel-forming pulse and the LWFA drive pulse, at backing pressures of 37–42 bar. The corresponding average neutral density was measured 8 mm above the nozzle orifice using the 'fluorescence method'[38], which compares the fluorescence of the Bessel focus over the gas jet with known neutral-density fluorescence signals generated in helium backfill (measured using a helium-calibrated pressure gauge). The resulting density range is $(1.30 - 1.45) \times 10^{18}$ cm^{-3}, with standard

Downloaded from https://www.cambridge.org/core. 19 Nov 2026 at 08:25:42, subject to the Cambridge Core terms of use.

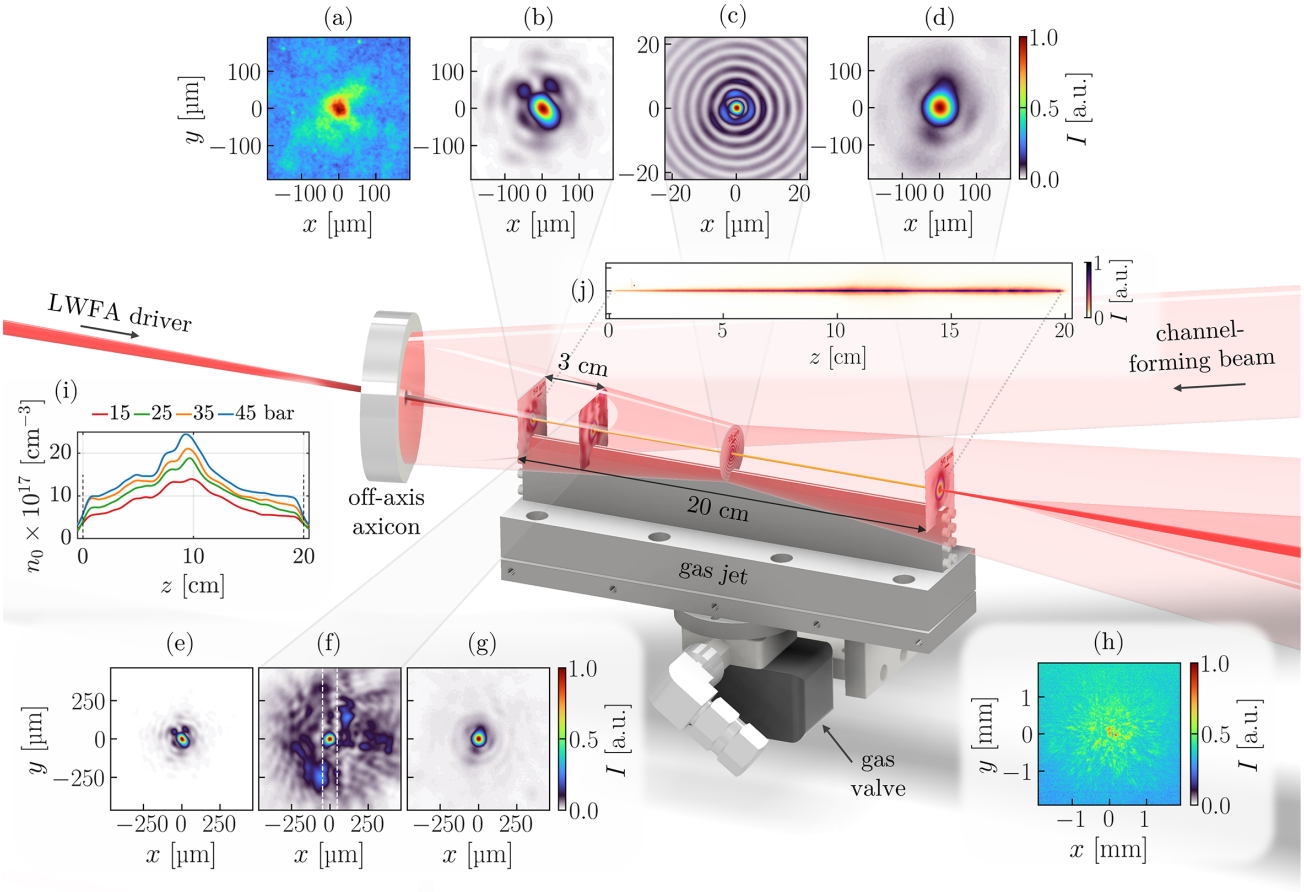


Figure 5. Guiding overview illustrating the interaction between the LWFA drive beam and the channel-forming beam, with the plasma column (yellow) highlighted between the focal plane and the waveguide exit plane above a 20 cm gas jet. (a) High-power focal-spot diagnostic image taken through the gas sheet during active guiding, used for online alignment monitoring. (b) High-power focal spot in vacuum, recorded using the focal-spot diagnostic camera. (c) Bessel beam focal spot, measured with a CMOS camera with 5× magnification objective. (d) Image of a guided mode exiting the 20 cm plasma waveguide acquired by the guided-mode diagnostic camera when the drive beam is successfully coupled into the waveguide. (e) Zoomed-out high-power focal-spot image, the same as in (b) for comparison with (f). (f) Guided mode exiting the 3 cm plasma waveguide using a short 3 cm gas jet (see Figure 7), showing leaky modes[39] surrounding the guided beam. (g) Zoomed-out guided mode exiting the 20 cm plasma waveguide, the same as in (d). (h) Guided-mode image recorded when the drive beam misses the waveguide entrance due to laser-pointing jitter. (i) Axial neutral-gas density profiles as a function of backing pressure, measured via helium fluorescence induced by J_0 Bessel beam ionization of the gas sheet 8 mm above the nozzle orifice with a 10 ms valve-opening time. The neutral density was calibrated using known helium backfill in the chamber[38]. (j) Top-view fluorescence image of the helium plasma channel generated by the off-axis axicon-produced J_0 Bessel beam. Images (a)–(h) and (j) are individually normalized.

deviation of 4×10^{17} cm^{-3} along the gas jet. The fluorescence measurement shown in Figure 5(i) was performed using the side-view diagnostic described in Section 2, where helium fluorescence was induced by J_0 Bessel beam ionization of the gas sheet.

Under these conditions, a 1% nitrogen–helium mixture filled the entire gas jet, enabling ionization injection over an extended longitudinal region of the plasma channel. The plasma channel size was controlled by adjusting the delay for hydrodynamic expansion, with optimal guiding occurring when the channel supported a matched mode waist $w_{ch} \approx w_0 \approx 32$ µm. The resulting electron spectra were typically broadband, with a mean electron energy of approximately equal to 3.5 GeV and high-energy features extending up to approximately 5 GeV (see Figure 8). Based on FLUKA[69–72] Monte Carlo simulations (version 4-3.4) of the 1 mm slit spectrometer setup, the uncertainty in the reconstructed electron energy is estimated to be approximately 15% at 3.5 GeV and approximately 20% at 5 GeV. The maximum observed electron energy is governed by the fraction of laser energy coupled into the plasma waveguide, the resulting effective acceleration length and the achievable accelerating field under the present laser and plasma conditions. For the measured L3 laser parameters on target ($a_0 = 2.55$) and assuming a plasma electron density of 2.7×10^{17} cm^{-3} (corresponding to $\sim 5\times$ lower on-axis density compared to the measured neutral density on target), the expected accelerating gradient is of the order of 38 GV/m, consistent with wakefield amplitudes reported in similar experiments operating in this parameter regime[25]. Ionization injection is most efficient during Stage II mode beating [39], which, under the present channel conditions, occurs approximately 5 cm

Downloaded from https://www.cambridge.org/core. 19 Nov 2026 at 08:25:42, subject to the Cambridge Core terms of use.

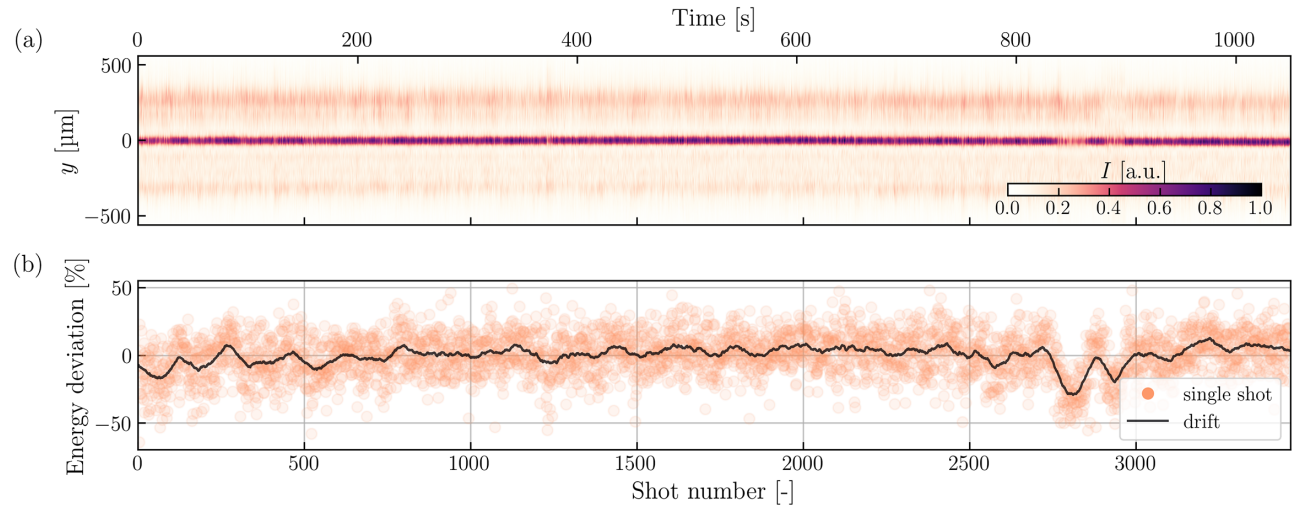


Figure 6. High-repetition-rate guiding results. (a) Evolution of the guided mode over approximately 20 minutes of operation at 3.3 Hz. Each shot is represented by a line-averaged intensity profile taken from a fixed region centered on the guided mode. (b) Evolution of the guided energy deviation within a beam radius ($1/e^2$), together with the energy drift calculated as a moving average over a 60-shot window.

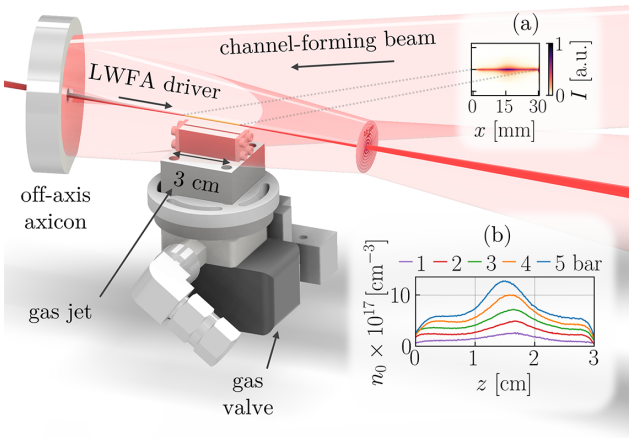


Figure 7. High-repetition-rate guiding overview illustrating the setup used with a 3 cm slit nozzle. (a) Normalized top-view fluorescence image of the 3 cm helium plasma channel. (b) Axial neutral-gas density profiles measured 5 mm above the nozzle orifice with a 2 ms valve-opening time as a function of backing pressure, measured via a top-view fluorescence diagnostic.

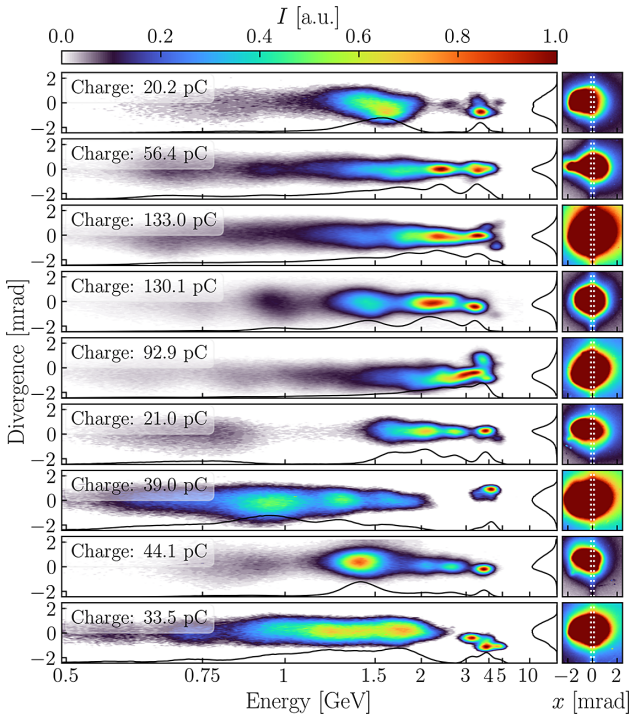


Figure 8. Selection of normalized high-energy electron spectra obtained during acceleration in a 20 cm nozzle at 0.2 Hz with a backing pressure of 37–42 bar. Each spectrum is accompanied by a corresponding pointing image, with the 1 mm spectrometer slit indicated by white dashed lines. Black curves at the bottom and right-hand side of each spectrum represent the signal integrated over divergence and energy axes, respectively.

into the gas target, limiting the effective acceleration length to approximately 15 cm. Using Lu scaling[73] with $a_0 = 2.55$, $\tau_{\mathrm{FWHM}} = 30.4$ fs, $w_0 = 32.1$ μm, $n_e = 2.7 \times 10^{17}$ cm^{-3} and a corresponding dephasing length $l_{\mathrm{deph}} = 15$ cm, the expected maximum electron energy is 5.5 GeV, consistent with the measured results.

Each spectrum in Figure 8 is shown together with the corresponding electron-beam pointing image recorded at the entrance of the magnetic spectrometer, where the 1 mm entrance slit is indicated by a dashed line. The accelerated electron beams exhibited characteristic features of self-waveguided propagation, including stable pointing and low divergence, with typical divergences of 1.2 ± 0.3 mrad (FWHM) for electron energies above 0.5 GeV and less than 0.6 mrad for electrons exceeding 3 GeV. Shot-to-shot variations in electron beam pointing along the axis perpendicular to the driver laser polarization, inferred from spectra above 0.5 GeV, were approximately equal to 0.35 mrad. This value is obtained by analyzing all shots from Figure 9(a), integrating the charge along the energy axis and calculating the centroid position for each shot. The resulting distribution is presented as a histogram in Figure 9(b)

Downloaded from https://www.cambridge.org/core. 19 Nov 2026 at 08:25:42, subject to the Cambridge Core terms of use.

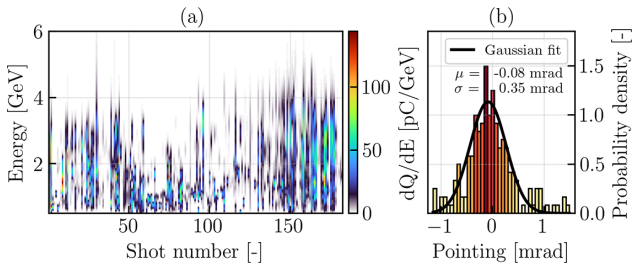


Figure 9. Statistical analysis of electron beam stability. (a) Evolution and distribution of the electron beam energy over multiple data sets acquired during optimization. (b) Statistical distribution of the electron beam pointing along the axis perpendicular to the driver laser polarization, shown as a probability-density histogram with a Gaussian fit.

and fitted with a normal (Gaussian) distribution, yielding $\mu = -0.08$ mrad and $\sigma = 0.35$ mrad. The electron spectra exhibited multi-peaked structures, consistent with mode-beating-induced ionization injection occurring at multiple longitudinal positions along the plasma channel[25,39].

The reported accelerated charge is obtained by integrating the signal measured by the electron spectrometer and therefore represents a lower bound on the total charge, as a significant fraction of the beam does not pass through the slit collimator. The uncertainty in the absolute charge measurement is estimated to be of the order of 15%−25%, primarily due to systematic effects in the spectrometer response, energy-dependent detector sensitivity and secondary particle production. Shot-to-shot variations in charge and spectral shape arise from laser-pointing fluctuations characterized by a standard deviation of approximately equal to 17 μm, which affects laser–channel coupling and leads to variations of approximately 30% in guided energy, as well as from injection dynamics and variations in the transverse electron-beam profile. Under otherwise identical experimental conditions, high-energy electron acceleration was achieved in approximately 40% of laser shots.

The electron beam energy evolution over multiple data sets acquired during optimization (e.g., delay between pulses, backing pressure and group delay dispersion (GDD)) is shown in Figure 9(a). The analysis includes all successfully accelerated electron beams with charge exceeding 0.5 pC transmitted through the spectrometer slit to the detector.

Additional acceleration experiments were carried out using 10% nitrogen–helium and 5% argon–helium mixtures to investigate the influence of dopant concentration and ionization potential on the injection dynamics.

5. Discussion

The results demonstrate that the all-reflective optical setup with an OAA provides stable and efficient guiding of high-power femtosecond laser pulses in helium, achieving both high-repetition-rate operation (3.3 Hz) and multi-GeV electron acceleration (0.2 Hz). The use of reflective components throughout the beamline eliminates thermally induced distortions typical of transmissive optics and could enhance stability during extended operation. In particular, the OAA configuration minimizes back-reflections and enables straightforward alignment – a crucial advantage for high-average-power systems and long-duration experimental campaigns.

Compared with previous implementations of self-waveguiding and optical-field-ionized plasma channels, our approach streamlines the self-waveguided LWFA scheme, eliminating the past requirements of additional compressors or multi-beam synchronization. The combination of post-compressor beam splitting and all-reflective optics allows the channel-forming beam to be derived directly from the main pulse without compromising pulse duration or spatial phase quality. This technique thus provides an accessible route toward stable and repeatable plasma guiding, fully compatible with existing user-facility laser architectures.

The observed guiding of petawatt-class laser pulses at 3.3 Hz over centimeter-scale distances confirms the robustness of OFI-generated plasma channels even at high repetition rates, consistent with prior low-energy studies. Furthermore, the electron acceleration experiments at 0.2 Hz demonstrate that this method can produce substantial electron energy gain, confirming its suitability for long plasma channels and higher drive-pulse energies. The use of helium, rather than hydrogen, simplifies gas handling and reduces operational hazards while maintaining efficient ionization and wake excitation.

6. Conclusion

We have demonstrated a high-repetition-rate, all-reflective laser guiding and electron acceleration setup employing an off-axis reflective axicon in helium plasma. The system supports stable optical guiding at 3.3 Hz and enables acceleration of electron beams to energies of approximately 5 GeV at 0.2 Hz, limited by the available laser parameters. This represents the first implementation of self-waveguiding in helium using a fully reflective optical system. The configuration preserves femtosecond pulse duration, minimizes nonlinear distortions and enhances reproducibility during extended operation.

The simplicity and robustness of this approach make it highly attractive for deployment in user facilities where modifications to the main laser system are constrained. Beyond serving as a compact and efficient method for high-energy electron acceleration, the presented scheme provides a foundation for future high-repetition-rate plasma accelerators and for the development of laser-driven secondary radiation sources, including compact X-ray and positron sources. Future work will focus on extending the plasma channel length, achieving higher-repetition-rate electron acceleration with petawatt-class lasers and integrating advanced

Downloaded from https://www.cambridge.org/core. 19 Nov 2026 at 08:25:42, subject to the Cambridge Core terms of use.

diagnostics and feedback control for real-time optimization of guiding and acceleration.

Acknowledgements

We sincerely thank the L3 laser team for providing the laser beam and their support during the experiments. We thank John J. Felice for helpful contributions to this study. This work was supported by the National Science Foundation and Czech Science Foundation under NSF-GACR collaborative Grant No. 2206059 from the Czech Science Foundation Grant No. 22-42963L. This work was supported by the U.S. Department of Energy (DE-SC0015516, LaserNetUS DE-SC0019076/FWP#SCW1668, and DE-SC0011375) and the Defense Advanced Research Projects Agency (DARPA) under the Muons for Science and Security Program. E. Rockafellow was supported by NSF GRFP (Grant No. DGE 1840340).

References

1. T. Tajima and J. M. Dawson, Phys. Rev. Lett. **43**, 267 (1979).
2. M. Galletti, R. Assmann, M. E. Couprie, M. Ferrario, L. Giannessi, A. Irman, R. Pompili, and W. Wang, Nat. Photonics **18**, 780 (2024).
3. W. Wang, K. Feng, L. Ke, C. Yu, Y. Xu, R. Qi, Y. Chen, Z. Qin, Z. Zhang, M. Fang, J. Liu, K. Jiang, H. Wang, C. Wang, X. Yang, F. Wu, Y. Leng, J. Liu, R. Li, and Z. Xu, Nature **595**, 516 (2021).
4. T. André, I. A. Andriyash, A. Loulergue, M. Labat, E. Roussel, A. Ghaith, M. Khojoyan, C. Thaury, M. Valléau, F. Briquez, F. Marteau, K. Tavakoli, P. N'Gotta, Y. Dietrich, G. Lambert, V. Malka, C. Benabderrahmane, J. Vétéran, L. Chapuis, T. E. Ajjouri, M. Sebdaoui, N. Hubert, O. Marcouillé, P. Berteaud, N. Leclercq, M. E. Ajjouri, P. Rommeluère, F. Bouvet, J.-P. Duval, C. Kitegi, F. Blache, B. Mahieu, S. Corde, J. Gautier, K. T. Phuoc, J. P. Goddet, A. Lestrade, C. Herbeaux, C. Évain, C. Szwaj, S. Bielawski, A. Tafzi, P. Rousseau, S. Smartsev, F. Polack, D. Dennetière, C. Bourassin-Bouchet, C. De Oliveira, and M.-E. Couprie, Nat. Commun. **9**, 1334 (2018).
5. G. Sarri, W. Schumaker, A. Di Piazza, M. Vargas, B. Dromey, M. E. Dieckmann, V. Chvykov, A. Maksimchuk, V. Yanovsky, Z. H. He, B. X. Hou, J. A. Nees, A. G. R. Thomas, C. H. Keitel, M. Zepf, and K. Krushelnick, Phys. Rev. Lett. **110**, 255002 (2013).
6. G. Sarri, K. Poder, J. M. Cole, W. Schumaker, A. Di Piazza, B. Reville, T. Dzelzainis, D. Doria, L. A. Gizzi, G. Grittani, S. Kar, C. H. Keitel, K. Krushelnick, S. Kuschel, S. P. D. Mangles, Z. Najmudin, N. Shukla, L. O. Silva, D. Symes, A. G. R. Thomas, M. Vargas, J. Vieira, and M. Zepf, Nat. Commun. **6**, 6747 (2015).
7. S. Corde, K. T. Phuoc, G. Lambert, R. Fitour, V. Malka, A. Rousse, A. Beck, and E. Lefebvre, Rev. Mod. Phys. **85**, 1 (2013).
8. W. Yan, C. Fruhling, G. Golovin, D. Haden, J. Luo, P. Zhang, B. Zhao, J. Zhang, C. Liu, M. Chen, S. Chen, S. Banerjee, and D. Umstadter, Nat. Photonics **11**, 514 (2017).
9. M. Mirzaie, C. I. Hojbota, D. Y. Kim, V. B. Pathak, T. G. Pak, C. M. Kim, H. W. Lee, J. W. Yoon, S. K. Lee, Y. J. Rhee, M. Vranic, Ó. Amaro, K. Y. Kim, J. H. Sung, and C. H. Nam, Nat. Photonics **18**, 1212 (2024).
10. J. M. Cole, K. T. Behm, E. Gerstmayr, T. G. Blackburn, J. C. Wood, C. D. Baird, M. J. Duff, C. Harvey, A. Ilderton, A. S. Joglekar, K. Krushelnick, S. Kuschel, M. Marklund, P. McKenna, C. D. Murphy, K. Poder, C. P. Ridgers, G. M. Samarin, G. Sarri, D. R. Symes, A. G. R. Thomas, J. Warwick, M. Zepf, Z. Najmudin, and S. P. D. Mangles, Phys. Rev. X **8**, 011020 (2018).
11. W. Dreesen, J. A. Green, M. Browder, J. Wood, D. Schwellenbach, T. Ditmire, G. Tiwari, and C. Wagner, in *IEEE Nuclear Science Symposium and Medical Imaging Conference (NSS/MIC)* (2014), p. 1.
12. F. Zhang, L. Deng, Y. Ge, J. Wen, B. Cui, K. Feng, H. Wang, C. Wu, Z. Pan, H. Liu, Z. Deng, Z. Zhang, L. Chen, D. Yan, L. Shan, Z. Yuan, C. Tian, J. Qian, J. Zhu, Y. Xu, Y. Yu, X. Zhang, L. Yang, W. Zhou, Y. Gu, W. Wang, Y. Leng, Z. Sun, and R. Li, Nat. Phys. **21**, 1050 (2025).
13. D. Terzani, S. Kisyov, S. Greenberg, L. Le Pottier, M. Mironova, A. Picksley, J. Stackhouse, R. L. Hai-En Tsai, E. Rockafellow, B. Miao, J. E. Shrock, T. Heim, M. Garcia-Sciveres, C. Benedetti, J. Valentine, H. M. Milchberg, K. Nakamura, A. J. Gonsalves, J. van Tilborg, C. B. Schroeder, E. Esarey, and C. G. R. Geddes, Phys. Rev. Accel. Beams **28**, 103401 (2025).
14. K. Poder, M. Tamburini, G. Sarri, A. Di Piazza, S. Kuschel, C. D. Baird, K. Behm, S. Bohlen, J. M. Cole, D. J. Corvan, M. Duff, E. Gerstmayr, C. H. Keitel, K. Krushelnick, S. P. D. Mangles, P. McKenna, C. D. Murphy, Z. Najmudin, C. P. Ridgers, G. M. Samarin, D. R. Symes, A. G. R. Thomas, J. Warwick, and M. Zepf, Phys. Rev. X **8**, 031004 (2018).
15. A. Gonoskov, T. G. Blackburn, M. Marklund, and S. S. Bulanov, Rev. Mod. Phys. **94**, 045001 (2022).
16. C. J. Zhang, J. F. Hua, Y. Wan, C.-H. Pai, B. Guo, J. Zhang, Y. Ma, F. Li, Y. P. Wu, H.-H. Chu, Y. Q. Gu, X. L. Xu, W. B. Mori, C. Joshi, J. Wang, and W. Lu, Phys. Rev. Lett. **119**, 064801 (2017).
17. Y. Wan, S. Tata, O. Seemann, E. Y. Levine, S. Smartsev, E. Kroupp, and V. Malka, Light Sci. Appl. **12**, 116 (2023).
18. B. K. Russell, P. T. Campbell, Q. Qian, J. A. Cardarelli, S. S. Bulanov, S. V. Bulanov, G. M. Grittani, D. Seipt, L. Willingale, and A. G. R. Thomas, Phys. Plasmas **30**, 093105 (2023).
19. L. Labate, D. Palla, D. Panetta, F. Avella, F. Baffigi, F. Brandi, F. Di Martino, L. Fulgentini, A. Giulietti, P. Köster, D. Terzani, P. Tomassini, C. Traino, and L. A. Gizzi, Sci. Rep. **10**, 17307 (2020).
20. Z. Guo, S. Liu, B. Zhou, J. Liu, H. Wang, Y. Pi, X. Wang, Y. Mo, B. Guo, J. Hua, Y. Wan, and W. Lu, Nat. Commun. **16**, 1895 (2025).
21. B. Zhou, Z. Guo, Y. Wan, S. Liu, B. Peng, J. Hua, and W. Lu, Phys. Rev. Accel. Beams **28**, 101304 (2025).
22. A. Degiovanni, W. Wuensch, and J. G. Navarro, Phys. Rev. Accel. Beams **19**, 032001 (2016).
23. W. P. Leemans, B. Nagler, A. J. Gonsalves, C. Tóth, K. Nakamura, C. G. R. Geddes, E. Esarey, C. B. Schroeder, and S. M. Hooker, Nat. Phys. **2**, 696 (2006).
24. C. E. Clayton, J. E. Ralph, F. Albert, R. A. Fonseca, S. H. Glenzer, C. Joshi, W. Lu, K. A. Marsh, S. F. Martins, W. B. Mori, A. Pak, F. S. Tsung, B. B. Pollock, J. S. Ross, L. O. Silva, and D. H. Froula, Phys. Rev. Lett. **105**, 105003 (2010).
25. B. Miao, J. E. Shrock, L. Feder, R. C. Hollinger, J. Morrison, R. Nedbailo, A. Picksley, H. Song, S. Wang, J. J. Rocca, and H. M. Milchberg, Phys. Rev. X **12**, 031038 (2022).
26. C. Aniculaesei, T. Ha, S. Yoffe, L. Labun, S. Milton, E. McCary, M. M. Spinks, H. J. Quevedo, O. Z. Labun, R. Sain, A. Hannasch, R. Zgadzaj, I. Pagano, J. A. Franco-Altamirano, M. L. Ringuette, E. Gaul, S. V. Luedtke, G.

Downloaded from https://www.cambridge.org/core. 19 Nov 2026 at 08:25:42, subject to the Cambridge Core terms of use.

Tiwari, B. Ersfeld, E. Brunetti, H. Ruhl, T. Ditmire, S. Bruce, M. E. Donovan, M. C. Downer, D. A. Jaroszynski, and B. M. Hegelich, Matter Radiat. Extreme. **9**, 014001 (2023).
27. C. B. Schroeder, E. Esarey, C. G. R. Geddes, C. Benedetti, and W. P. Leemans, Phys. Rev. ST Accel. Beams **13**, 101301 (2010).
28. H. T. Kim, K. H. Pae, H. J. Cha, I. J. Kim, T. J. Yu, J. H. Sung, S. K. Lee, T. M. Jeong, and J. Lee, Phys. Rev. Lett. **111**, 165002 (2013).
29. A. Morozov, A. Goltsov, Q. Chen, M. Scully, and S. Suckewer, Phys. Plasmas **25**, 053110 (2018).
30. N. Lemos, L. Cardoso, J. Geada, G. Figueira, F. Albert, and J. M. Dias, Sci. Rep. **8**, 3165 (2018).
31. R. J. Shalloo, C. Arran, L. Corner, J. Holloway, J. Jonnerby, R. Walczak, H. M. Milchberg, and S. M. Hooker, Phys. Rev. E **97**, 053203 (2018).
32. S. Smartsev, C. Caizergues, K. Oubrerie, J. Gautier, J.-P. Goddet, A. Tafzi, K. T. Phuoc, V. Malka, and C. Thaury, Opt. Lett. **44**, 3414 (2019).
33. R. J. Shalloo, C. Arran, A. Picksley, A. von Boetticher, L. Corner, J. Holloway, G. Hine, J. Jonnerby, H. M. Milchberg, C. Thornton, R. Walczak, and S. M. Hooker, Phys. Rev. Accel. Beams **22**, 041302 (2019).
34. B. Miao, L. Feder, J. E. Shrock, A. Goffin, and H. M. Milchberg, Phys. Rev. Lett. **125**, 074801 (2020).
35. L. Feder, B. Miao, J. E. Shrock, A. Goffin, and H. M. Milchberg, Phys. Rev. Res. **2**, 043173 (2020).
36. A. Picksley, A. Alejo, J. Cowley, N. Bourgeois, L. Corner, L. Feder, J. Holloway, H. Jones, J. Jonnerby, H. M. Milchberg, L. R. Reid, A. J. Ross, R. Walczak, and S. M. Hooker, Phys. Rev. Accel. Beams **23**, 081303 (2020).
37. A. Picksley, A. Alejo, R. J. Shalloo, C. Arran, A. von Boetticher, L. Corner, J. A. Holloway, J. Jonnerby, O. Jakobsson, C. Thornton, R. Walczak, and S. M. Hooker, Phys. Rev. E **102**, 053201 (2020).
38. J. E. Shrock, B. Miao, L. Feder, and H. M. Milchberg, Phys. Plasmas **29**, 073101 (2022).
39. J. E. Shrock, E. Rockafellow, B. Miao, M. Le, R. C. Hollinger, S. Wang, A. J. Gonsalves, A. Picksley, J. J. Rocca, and H. M. Milchberg, Phys. Rev. Lett. **133**, 045002 (2024).
40. B. Miao, E. Rockafellow, J. E. Shrock, S. W. Hancock, D. Gordon, and H. M. Milchberg, Phys. Rev. Accel. Beams **27**, 081302 (2024).
41. A. Picksley, J. Stackhouse, C. Benedetti, K. Nakamura, H. E. Tsai, R. Li, B. Miao, J. E. Shrock, E. Rockafellow, H. M. Milchberg, C. B. Schroeder, J. van Tilborg, E. Esarey, C. G. R. Geddes, and A. J. Gonsalves, Phys. Rev. Lett. **133**, 255001 (2024).
42. E. Rockafellow, B. Miao, J. E. Shrock, A. Sloss, M. S. Le, S. W. Hancock, S. Zahedpour, R. C. Hollinger, S. Wang, J. King, P. Zhang, J. Šišma, G. M. Grittani, R. Versaci, D. F. Gordon, G. J. Williams, B. A. Reagan, J. J. Rocca, and H. M. Milchberg, Phys. Plasmas **32**, 053102 (2025).
43. E. Rockafellow, J. E. Shrock, B. Miao, A. J. Sloss, M. S. Le, S. W. Hancock, S. Zahedpour, R. C. Hollinger, S. Wang, J. King, P. Zhang, J. Šišma, G. M. Grittani, R. Versaci, D. F. Gordon, G. J. Williams, B. A. Reagan, J. J. Rocca, and H. M. Milchberg, Nucl. Instrum. Methods Phys. Res., Sect. A **1077**, 170586 (2025).
44. N. A. Bobrova, A. A. Esaulov, J.-I. Sakai, P. V. Sasorov, D. J. Spence, A. Butler, S. M. Hooker, and S. V. Bulanov, Phys. Rev. E **65**, 016407 (2001).
45. A. Butler, D. J. Spence, and S. M. Hooker, Phys. Rev. Lett. **89**, 185003 (2002).
46. S. Karsch, J. Osterhoff, A. Popp, T. P. Rowlands-Rees, Z. Major, M. Fuchs, B. Marx, R. Hörlein, K. Schmid, L. Veisz, S. Becker, U. Schramm, B. Hidding, G. Pretzler, D. Habs, F. Grüner, F. Krausz, and S. M. Hooker, New J. Phys. **9**, 415 (2007).
47. T. P. Rowlands-Rees, C. Kamperidis, S. Kneip, A. J. Gonsalves, S. P. D. Mangles, J. G. Gallacher, E. Brunetti, T. Ibbotson, C. D. Murphy, P. S. Foster, M. J. V. Streeter, F. Budde, P. A. Norreys, D. A. Jaroszynski, K. Krushelnick, Z. Najmudin, and S. M. Hooker, Phys. Rev. Lett. **100**, 105005 (2008).
48. A. J. Gonsalves, K. Nakamura, J. Daniels, C. Benedetti, C. Pieronek, T. C. H. de Raadt, S. Steinke, J. H. Bin, S. S. Bulanov, J. van Tilborg, C. G. R. Geddes, C. B. Schroeder, C. Tóth, E. Esarey, K. Swanson, L. Fan-Chiang, G. Bagdasarov, N. Bobrova, V. Gasilov, G. Korn, P. Sasorov, and W. P. Leemans, Phys. Rev. Lett. **122**, 084801 (2019).
49. N. Tripathi, B. Miao, A. Sloss, E. Rockafellow, J. E. Shrock, S. W. Hancock, and H. M. Milchberg, Opt. Lett. **50**, 3441 (2025).
50. C. G. Durfee and H. M. Milchberg, Phys. Rev. Lett. **71**, 2409 (1993).
51. C. G. Durfee, J. Lynch, and H. M. Milchberg, Phys. Rev. E **51**, 2368 (1995).
52. P. B. Corkum, N. H. Burnett, and F. Brunel, Phys. Rev. Lett. **62**, 1259 (1989).
53. S. Lorenz, G. Grittani, E. Chacon-Golcher, C. M. Lazzarini, J. Limpouch, F. Nawaz, M. Nevrkla, L. Vilanova, and T. Levato, Matter Radiat. Extreme. **4**, 015401 (2019).
54. B. Miao, J. E. Shrock, E. Rockafellow, A. J. Sloss, and H. M. Milchberg, Rev. Sci. Instrum. **96**, 043003 (2025).
55. C. V. Pieronek, A. J. Gonsalves, C. Benedetti, S. S. Bulanov, J. van Tilborg, J. H. Bin, K. K. Swanson, J. Daniels, G. A. Bagdasarov, N. A. Bobrova, V. A. Gasilov, G. Korn, P. V. Sasorov, C. G. R. Geddes, C. B. Schroeder, W. P. Leemans, and E. Esarey, Phys. Plasmas **27**, 093101 (2020).
56. B. Miao, L. Feder, J. E. Shrock, and H. M. Milchberg, Opt. Express **30**, 11360 (2022).
57. M. Turner, S. S. Bulanov, C. Benedetti, A. J. Gonsalves, W. P. Leemans, K. Nakamura, J. van Tilborg, C. B. Schroeder, C. G. R. Geddes, and E. Esarey, Eur. Phys. J. D **76**, 205 (2022).
58. P. Boucher, J. D. Hoyo, C. Billet, O. Pinel, G. Labroille, and F. Courvoisier, Appl. Opt. **57**, 6725 (2018).
59. X. M. Tong and C. D. Lin, J. Phys. B Atomic Mol. Phys. **38**, 2593 (2005).
60. A. Alejo, J. Cowley, A. Picksley, R. Walczak, and S. M. Hooker, Phys. Rev. Accel. Beams **25**, 011301 (2022).
61. C. M. Lazzarini, L. V. Goncalves, G. M. Grittani, S. Lorenz, M. Nevrkla, P. Valenta, T. Levato, S. V. Bulanov, and G. Korn, Int. J. Modern Phys. A **34**, 1943010 (2019).
62. T. Willemsen, U. Chaulagain, I. Havlíčková, S. Borneis, W. Ebert, H. Ehlers, M. Gauch,. Groß, D. Kramer, T. Laštovička, J. Nejdl, B. Rus, K. Schrader, T. Tolenis, F. Vaněk, P. K. Velpula, and S. Weber, Opt. Express **30**, 6129 (2022).
63. I. Zymak, M. Favetta, G. M. Grittani, C. M. Lazzarini, G. Tassielli, A. Grenfell, L. Goncalves, S. Lorenz, V. Sluková, F. Vitha, R. Versaci, E. Chacon-Golcher, M. Nevrkla, J. Šišma, R. Antipenkov, V. Šobr, W. Szuba, T. Staufer, F. Grüner, L. Lapadula, E. Ranieri, M. Piombino, N. A. M. Hafz, C. Kamperidis, D. Papp, S. Mondal, P. Bakule, and S. V. Bulanov. Photonics **11**, 1208 (2024).
64. J. M. Auerbach and V. P. Karpenko, Appl. Opt. **33**, 3179 (1994).
65. https://www.lighttrans.com/products-services/learning/users-manual.html.
66. C. Iaconis and I. A. Walmsley, Opt. Lett. **23**, 792 (1998).
67. T. M. Antonsen, Jr. and P. Mora, Phys. Rev. Lett. **74**, 4440 (1995).
68. T. R. Clark and H. M. Milchberg, Phys. Rev. E **61**, 1954 (2000).
69. G. Battistoni, T. Boehlen, F. Cerutti, P. W. Chin, L. S. Esposito, A. Fassò, A. Ferrari, A. Lechner, A. Empl, A. Mairani,

Downloaded from https://www.cambridge.org/core. 19 Nov 2026 at 08:25:42, subject to the Cambridge Core terms of use.

A. Mereghetti, P. G. Ortega, J. Ranft, S. Roesler, P. R. Sala, V. Vlachoudis, and G. Smirnov, Ann. Nucl. Energy **82**, 10 (2015).
70. C. Ahdida, D. Bozzato, D. Calzolari, F. Cerutti, N. Charitonidis, A. Cimmino, A. Coronetti, G. L. D'Alessandro, A. Donadon Servelle, L. S. Esposito, R. Froeschl, R. García Alía, A. Gerbershagen, S. Gilardoni, D. Horváth, G. Hugo, A. Infantino, V. Kouskoura, A. Lechner, B. Lefebvre, G. Lerner, M. Magistris, A. Manousos, G. Moryc, F. Ogallar Ruiz, F. Pozzi, D. Prelipcean, S. Roesler, R. Rossi, M. Sabaté Gilarte, F. Salvat Pujol, P. Schoofs, V. Stránský, C. Theis, A. Tsinganis, R. Versaci, V. Vlachoudis, A. Waets, and M. Widorski, Front. Phys. **9**, 2021 (2022).
71. A. Donadon, G. Hugo, C. Theis, and V. Vlachoudis, EPJ Web Conf. **302**, 11005 (2024).
72. G. Hugo, C. Ahdida, D. Bozzato, D. Calzolari, F. Cerutti, A. Ciccotelli, A. Cimmino, A. Devienne, A. Donadon Servelle, P. K. Dyrcz, L. Salvatore Esposito, A. Formento, R. Froeschl, R. García Alía, S. Gilardoni, A. Gomes, D. Horváth, B. Humann, A. Infantino, A. Lechner, B. Lefebvre, G. Lerner, T. Lorenzon, D. Lucsanyi, M. Magistris, S. Marin, G. Mazzola, S. Niang, E. Nowak, F. Ogallar Ruiz, J.-B. Potoine, F. Pozzi, D. Prelipcean, V. Rodin, S. Roesler, M. Sabaté Gilarte, M. Sacristan Barbero, F. Salvat Pujol, P. Schoofs, A.-G. Serban, I. Sharankov, C. Theis, M. Tisi, A. Tsinganis, R. Versaci, V. Vlachoudis, A. Waets, M. Widorski, and I. Zymak, EPJ Nuclear Sci. Technol. **10**, 20 (2024).
73. W. Lu, M. Tzoufras, C. Joshi, F. S. Tsung, W. B. Mori, J. Vieira, R. A. Fonseca, and L. O. Silva, Phys. Rev. ST Accel. Beams **10**, 061301 (2007).

Downloaded from https://www.cambridge.org/core. 19 Nov 2026 at 08:25:42, subject to the Cambridge Core terms of use.